Optical Spectroscopy and Crystal Field Studies of the Mn^{4+} Ion ($3d^3$) in the Double Perovskite $NaLaMgTeO_6$

Alok M. Srivastava[a], Mikhail G. Brik[b], Samuel J. Camardello[a], Holly A. Comanzo[a], and Florencio Garcia-Santamaria[a]

[a] GE Global Research, One Research Circle, Niskayuna, New York 12309, USA

[b] Institute of Physics, University of Tartu, Riia 142, Tartu 51014, Estonia

Reprint requests to Alok M. Srivastava. E-mail: srivastava@ge.com

Z. Naturforsch. **2014**, *69b*, 141 – 149 / DOI: 10.5560/ZNB.2014-3259
Received August 21, 2013

The spectroscopic properties of the Mn^{4+} ion ($3d^3$) in the double perovskite $NaLaMgTeO_6$ are reported in this work. Evidence is presented for the occupation by the Mn^{4+} ion of both the six coordinated Mg^{2+} and Te^{6+} sites in the host structure. The Mn^{4+} energy levels are calculated using the exchange charge model of crystal field theory for both occupied sites. The results of our calculations yield the crystal field splitting and Racah parameters of $Dq = 2008\ cm^{-1}$, $B = 790\ cm^{-1}$, $C = 2881\ cm^{-1}$, with $C/B = 3.65$ (Mg^{2+} site) and $Dq = 2008\ cm^{-1}$, $B = 790\ cm^{-1}$, $C = 2949\ cm^{-1}$, with $C/B = 3.73$ (Te^{6+} site). A cross-cutting comparative study of the variations in the crystal field splitting and the Racah parameters of the six-coordinated Mn^{4+} ion in a series of materials with the perovskite structure are presented.

Key words: Mn^{4+} Ion, Crystal Field Splitting, Perovskites, Optical Materials

Introduction

In recent years, we carried out detailed studies pertaining to the optical properties of the Mn^{4+} ion ($3d^3$ electronic configuration) in a wide variety of host materials with the goal of rationalizing the optical spectra as a function of the surroundings of the Mn^{4+} ion in the crystalline structure [1 – 6]. In many of these studies we have calculated the electronic energy levels of the Mn^{4+} ion and demonstrated that the results of our calculations are in good agreement with the experimental data. The results of our crystal field calculations permit the extraction of the three principal physical parameters of interest: (1) the crystal field splitting ($10Dq$) and, (2) the two Racah parameters, B and C (for the Coulomb interaction between the d electrons in the unfilled $3d$ shell). The prime goal of our program is to relate the variations in these parameters to changes in the "Mn^{4+}-ligand" bonding in the crystalline solids.

The electronic ground state of the Mn^{4+} ion ($^4A_{2g}$) and the lowest excited state (^2E) arise from the t_{2g}^3 configuration. The excitation/absorption spectra of the Mn^{4+} ion in oxidic matrices are usually dominated by the $O^{2-} \rightarrow Mn^{4+}$ charge transfer transition and the internal ($3d$-$3d$; broad band) $^4A_{2g} \rightarrow {}^4T_{2g}$ and $^4A_{2g} \rightarrow {}^4T_{1g}$ spin-allowed optical transitions. The Mn^{4+} emission corresponds with the $^2E_g \rightarrow {}^4A_{2g}$ spin-forbidden transition which is independent of the value of Dq/B in the theory of Tanabe and Sugano [7] and consists of sharp R-line emission with the associated vibronic band. The energy of the Mn^{4+} ^2E_g state is dependent on the covalence of the "Mn^{4+}-ligand" bonding in the crystalline solids. Of fundamental interest is the ability to tune the Mn^{4+} emission wavelength by altering the covalence of the "Mn^{4+}-ligand" bonding which is host structure-dependent [1].

Perovskites with the general formulation ABX_3 contain corner-shared BX_6 octahedral groups with the larger A cations in a body-centered position (coordination number of 12). Perovskites represent a versatile family of materials in which the compositions can be readily changed to vary the covalence of the "Mn^{4+}-ligand" bonding, which as discussed previously, influences the energy of the emitting ^2E_g state. Results pertaining to the calculation of the energy levels of the Mn^{4+} ion in perovskites such as $YAlO_3$ [8], $SrTiO_3$ [9] and $BaTiO_3$ [10] are available in the archival literature. In recent years, we have systematically explored the

optical properties of the Mn^{4+} ion in materials which crystallize with the perovskite structure. Thus, for example, we have provided the results of crystal field calculations of the Mn^{4+} energy level in the double perovskite Ba_2LaNbO_6 [4] and in rhombohedral and orthorhombic perovskites, $LaAlO_3$ [6] and $CaZrO_3$ [11], respectively.

The spectroscopic properties of the Mn^{4+} ion in the $NaLaMgTeO_6$ double perovskite were investigated in this work. The electronic energy levels of the Mn^{4+} ion are calculated by the exchange charge model of crystal field theory and compared with the experimental data. Further, we also provide a comparative study of the spectroscopic properties of the Mn^{4+} ions in different perovskite structures and suggest a criterion to relate the energy position of the ^2E state to the degree of covalence in a particular host. The degree of covalence is quantified by ratios of the Racah parameters B and C in a crystal to those for Mn^{4+} ion in the free state.

Experimental

The compound $NaLaMgTeO_6$ activated with Mn^{4+} (0.005) was prepared by the solid-state reaction technique. Commercially obtained La_2O_3 was heated to 1000 °C in an atmosphere of nitrogen and subsequently stored in a dry box because it is known to pick up water and CO_2 from the atmosphere. The dried La_2O_3 was mixed with MgO, TeO_2 and Na_2CO_3 (10 mole-% excess) and heated to 900 °C in a covered crucible in air. The resulting powder was re-blended and heated at 1000 °C for a period of 10 hours. X-Ray diffraction data was characteristic of the monoclinic perovskite structure, indicating the formation of a single-phase material.

Low-temperature luminescence measurements were carried out as previously described [12]. All spectra have been corrected for the wavelength-dependent variations in the Xe lamp intensity and for the photomultiplier response. The room temperature diffuse reflectance of pure $NaLaMgTeO_6$ was measured on a Perkin-Elmer spectrometer. Photoluminescence decay curves at 12 K were measured by pressing the sample powder into a copper plaque that was then attached to a cryostat (Advance Research Systems, Inc.). The cryostat was evacuated with a turbo pump (HiCUBE, Pfeiffer) and cooled down for about one hour. A thermocouple attached to the plaque provided a reading of the sample temperature. The excitation radiation was produced by a microsecond Xe flashlamp (2 μs pulses at 10 Hz). The radiation was passed through a double monochromator that allows selecting the excitation wavelength (350 and 492 nm in our experiments) and led into an optical fiber to carry the signal to the sample. The radiation emitted by the sample was collected by a second optical fiber and taken to the spectrometer (FS920, Edinburgh Instruments, Inc.). The manufacturer software uses the multi-channel scaling technique to allow time-resolved measurements.

Results and Discussions

Crystal structure of NaLaMgTeO$_6$

The compound $NaLaMgTeO_6$ [13] belongs to the family of materials that crystallize in a distorted perovskite structure with space group $P12_1/m1$ (no. 11). The lattice constants are $a = 5.5526$, $b = 5.5349$, $c = 7.9126$ Å, $\beta = 90.22°$, with two formula units per unit cell. Fig. 1 illustrates one unit cell of $NaLaMgTeO_6$.

The crystal structure of this perovskite simultaneously exhibits rock salt ordering of the B-site cations (Mg^{2+}, Te^{6+}) and layered ordering of the A-site cations (Na^+, La^{3+}) [13, 15, 16]. Both the B-site cations, Mg^{2+} and Te^{6+}, are in six-fold oxygen coordination (distorted octahedra). The Mg^{2+}–O^{2-} distances (all in Å) are as follows: 2.060 (×2), 2.044 (×2), 2.122 and 1.913. The O–Mg–O angles (which would all be 180° in the case of an ideal octahedron) are 163.9° (×2) and 175.9° (one angle). The Te^{6+}–O^{2-} distances (all in Å) are as follows: 1.990 (×2), 1.849 (×2), 1.920, 2.060. The O–Te–O angles formed by *trans* oxygen atoms and Te^{6+} ion are: 170.5° (×2) and 174.5° (one angle).

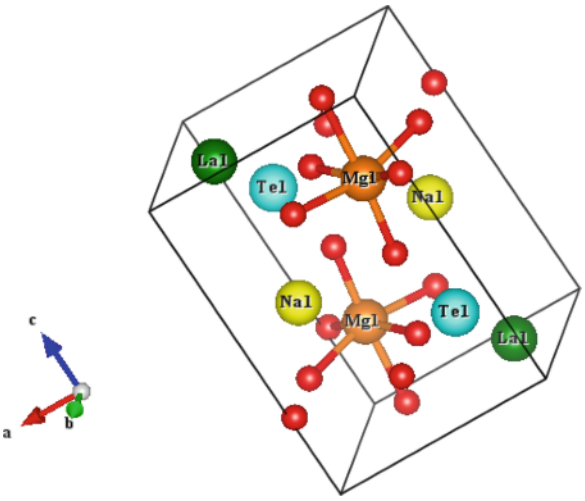

Fig. 1. The unit cell of $NaLaMgTeO_6$. The B-site Mg^{2+} and Te^{6+} cations are located inside the octahedra formed by the oxygen ions (drawn with VESTA [14]).

	$NaLaMgTeO_6$:Mn^{4+} (Mg^{2+} site)			$NaLaMgTeO_6$:Mn^{4+} (Te^{4+} site)		
	$B^k_{p,q}$	$B^k_{p,S}$	B^k_p			
B_2^{-2}	7.5	0	7.5	7.2	−0.5	6.7
B_2^{-1}	−7.9	0.3	−7.6	−8.1	−0.6	−8.7
B_2^0	703.1	1572.4	2275.5	−1184.8	−1738.2	−2923.0
B_2^1	−4080.1	−3637.4	−7717.5	2561.8	1139.0	3700.8
B_2^2	−3232.3	−2209.3	−5441.6	5164.0	3675.4	8839.4
B_4^{-4}	0	0	0	0	0	0
B_4^{-3}	0	0	0	0	0	0
B_4^{-2}	0	0	0	0	0	0
B_4^{-1}	0	0	0	0	0	0
B_4^0	443.0	4367.3	4810.3	612.6	3937.7	4550.3
B_4^1	−1510.8	−14935.0	−16445.8	1715.7	11569.2	13284.9
B_4^2	320.5	2947.7	3268.2	−151.1	−942.9	−1094.0
B_4^3	−1334.2	−13009.9	−14344.1	1219.2	8625.4	9844.6
B_4^4	−2314.8	−22563.5	−24878.3	−3623.1	−23864.9	−27488.0
B			790			790
C			2881			2949
G			10.02			6.77

Table 1. Crystal field (in Stevens normalization) and Racah parameters (in cm^{-1}) for Mn^{4+} in $NaLaMgTeO_6$. G is the dimensionless ECM parameter.

The ionic radii of the Mn^{4+}, Mg^{2+} and Te^{6+} ions are 0.53, 0.72 and 0.56 Å, respectively [17]. Thus the Mn^{4+} ion can occupy both the six-coordinated Mg^{2+} and Te^{6+} sites. If half of the Mn^{4+} ions substitute at the Mg^{2+} site and another half at the Te^{6+} site, there will be no requirement for charge compensation. Evidence will be presented for the occupation by the Mn^{4+} ion of both the six coordinated Mg^{2+} and Te^{6+} sites in the host structure.

Method of calculations

Crystal field theory allows the calculations of the energy levels of impurity ions with an unfilled d-shell in a crystal field of arbitrary symmetry by diagonalizing the following CF Hamiltonian [18],

$$H = \sum_{p=2,4} \sum_{k=-p}^{p} B^k_p O^k_p, \tag{1}$$

where O^k_p are the suitably chosen linear combinations of the irreducible tensor operators acting on the angular parts of the impurity ion's wave functions (exact definition of the operators used in the exchange charge model (ECM) can be found in ref. [18]), and B^k_p are the crystal field parameters (CFPs) which can be calculated from the crystal structure data. These entries include all the structural and geometrical information about the host structure which reflects the arrangement of the host ions around the impurity site. The Hamiltonian (Eq. 1) is defined in the space spanned by all wave functions of the free ion's LS terms (which arise due to the Coulomb interaction between electrons of an impurity ion). The ECM allows expressing the CFPs as a sum of two terms [18]:

$$B^k_p = B^k_{p,q} + B^k_{p,S}, \tag{2}$$

with

$$B^k_{p,q} = -K^k_p e^2 \langle r^p \rangle \sum_i q_i \frac{V^k_p(\theta_i, \varphi_i)}{R_i^{p+1}}, \tag{3}$$

and

$$B^k_{p,S} = K^k_p e^2 \frac{2(2p+1)}{5} \sum_i \left(G_s S(s)^2_i + G_\sigma S(\sigma)^2_i + \gamma_p G_\pi S(\pi)^2_i \right) \frac{V^k_p(\theta_i, \varphi_i)}{R_i}. \tag{4}$$

The first term $B^k_{p,q}$ is the point charge contribution to the CFPs, which arises from the electrostatic interaction between the central ion and the ions enumerated by index i with charges q_i and spherical coordinates R_i, θ_i, φ_i (with the reference system centered at the impurity ion itself). The averaged values $\langle r^p \rangle$, where r is the radial coordinate of the d electrons of the optical center (also known as the moment of the $3d$ electron density), can either be obtained from the literature or calculated numerically, using the radial parts of the corresponding ion's wave functions. The values of the numerical

factors K_p^k, γ_p, the expressions for the polynomials V_p^k and the definitions of the operators O_p^k can all be found in ref. [18] and thus are not shown here for the sake of brevity. The second term of Eq. 2, $B_{p,S}^k$, is proportional to the overlap between the wave functions of the central ion and the ligands and thus includes all covalent effects. The $S(s), S(\sigma), S(\pi)$terms correspond to the overlap integrals between the d functions of the central ion and p and $s$functions of the ligands: $S(s) = \langle d0|s0\rangle$, $S(\sigma) = \langle d0|p0\rangle$, $S(\pi) = \langle d1|p1\rangle$. The G_s, G_σ, G_π entries are dimensionless adjustable parameters of the model, whose values are determined by the positions of the first three absorption bands in the experimental spectrum. They can be approximated to a single value, *i. e.* $G_s = G_\sigma = G_\pi = G$, which then can be estimated from one (lowest in energy) absorption band only. This is usually a reasonable approximation [18]. The summation in Eq. 4 is extended only to the nearest neighbors of an impurity ion (*i. e.* six ligands in the case of an octahedral impurity center in $NaLaMgTeO_6$:Mn^{4+}), since the overlap with the ions from the further (second, third *etc.*) coordination spheres can be safely neglected.

The ECM employs a small number of fitting parameters and allows for calculating the crystal field parameters and energy levels of impurities in crystals without making any assumptions about the impurity center symmetry. The reliability and vitality of the ECM is confirmed by its success in calculating the energy level of the transition metal and rare earth ions [1–5, 18, 19].

Results of calculations: determination of the crystal field splitting (10 Dq) and the Racah parameters (B and C)

The low-temperature excitation and emission spectra of $NaLaMgTeO_6$ are shown in Figs. 2 and 3. The crystal structural data of ref. [13] were used to calculate the CFP values. The Mn^{4+}–O^{2-} overlap integrals were calculated numerically using the radial parts of the transition metal ions' and the O^{2-} anion wave functions that were taken from refs. [20, 21]. To ensure proper convergence of the crystal structure sums (especially for the second rank of CFPs, varying with the interatomic distance R as $1/R^3$), a large cluster consisting of 34 560 ions in $NaLaMgTeO_6$ was considered when calculating the energy levels of Mn^{4+} ions at both Mg^{2+} and Te^{6+} sites. Table 1 collects the calculated values of the non-zero CFPs for Mn^{4+} ions in $NaLaMgTeO_6$. To illustrate the role and significance of the exchange parameters of crystal field, point charge $B_{p,q}^k$ and exchange charge $B_{p,S}^k$ contributions to the total CFPs are shown separately. The second contribution to the CFPs is of paramount importance, being several times larger than the point charge term.

Table 2. Calculated and experimental energy levels (in cm^{-1}) for Mn^{4+} in $NaLaMgTeO_6$.

O_h group notation and "parent" LS term	Mg^{2+} site (calcd.)	Te^{6+} site (calcd.)	Exp.
$^4A_{2g}$ (^4F)	0	0	
^2E_g (^2G)	14 228	14 286	14 286
	14 341	14 287	
$^2T_{1g}$ (^2G)	14 697	14 528	
	14 946	15 454	
	15 305	15 962	
$^4T_{2g}$ (^4F)	19 461	18 235	20 080
	20 218	20 270	
	20 583	21 736	
$^2T_{2g}$ (^2G)	21 424	21 056	
	22 270	22 995	
	23 341	23 784	
$^4T_{1g}$ (^4F)	26 679	26 270	30 800
	28 213	28 712	
	31 187	30 301	
$^4T_{1g}$ (^4P)	42 949	41 172	
	44 445	44 164	
	47 343	48 767	

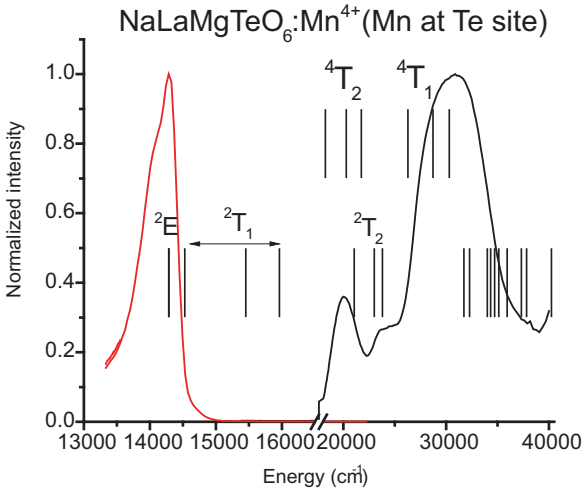

Fig. 2. Low-temperature ($T = 10$ K) emission (left; $\lambda_{ex} = 320$ nm) and excitation (right; $\lambda_{em} = 700$ nm) spectrum of $NaLaMgTeO_6$:Mn^{4+} in comparison with calculated energy levels of Mn^{4+} at the Te^{6+} position.

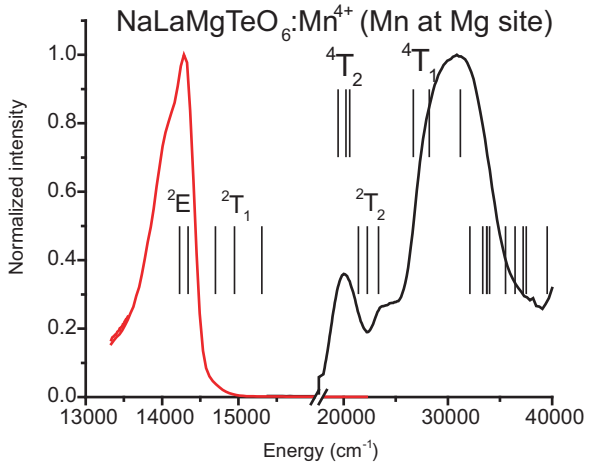

Fig. 3. Low-temperature ($T = 10$ K) emission (left; $\lambda_{ex} = 320$ nm) and excitation (right; $\lambda_{em} = 700$ nm) spectrum of $NaLaMgTeO_6$:Mn^{4+} in comparison with calculated energy levels of Mn^{4+} at the Mg^{2+} position.

The CF Hamiltonian (Eq. 1) with CFPs from Table 1 was diagonalized in the space spanned by 50 wave functions of all 8 LS terms (^{4}F, ^{4}P, ^{2}P, ^{2}D$_{1,2}$, ^{2}F, ^{2}G, ^{2}H) of the $3d^3$ electron configuration characteristic of Mn^{4+} ions. The spin-orbit interaction was neglected because the experimental spectra are broad and exhibit no clearly resolved fine structure that could be unambiguously taken as a manifestation of the spin-orbit interaction. The ECM parameter G was determined using the experimental data pertaining to the splitting of the ^{4}F ground term, in particular, from the energy position of the first absorption band in the experimental spectra; its values are also assembled in Table 1. The values of the Racah parameters B and C, which were chosen from the best agreement with experimental data, are also given in Table 1.

The calculated energy levels of the Mn^{4+} ion in $NaLaMgTeO_6$ are collected in Table 2. Figs. 2 and 3 visualize the correspondence between the results of the crystal field calculations and the experimental excitation spectrum. The two broad structureless bands in the excitation spectrum are ascribed to the spin-allowed transitions, $^4A_{2g}(^4F)$–$^4T_{2g}(^4F)$ (with its maximum at about 20 080 cm^{-1}) and $^4A_{2g}(^4F)$–$^4T_{1g}(^4F)$ (with its maximum at about 30 080 cm^{-1}). The absorption edge of the host structure (pure $NaLaMgTeO_6$) was estimated at 235 nm (42 553 cm^{-1}) from the room-temperature diffuse reflectance spectrum. A similar host structure absorption energy has been reported for other Te^{6+}-based materials such as $Gd_3Li_3Te_2O_{12}$ (garnet structure; 40 000 cm^{-1}) [22] and La_2TeO_6 (41 666 cm^{-1}) [23]. The absorption edge thus corresponds to the $O^{2-} \rightarrow Te^{6+}$ charge transfer transition. Since the host structure absorption occurs at 42 553 cm^{-1}, the strong band centered near 30 000 cm^{-1} in the excitation spectrum of $NaLaMgTeO_6$:Mn^{4+} (Figs. 2 and 3) is a superposition of the $O^{2-} \rightarrow Mn^{4+}$ charge transfer and the Mn^{4+} spin-allowed ($3d-3d$) transitions.

The strong sharp line at 14 705 cm^{-1} is assigned to the emission from the Mn^{4+} ^{2}E state. The strong intensity of the Mn^{4+} $^2E \rightarrow {}^4A_{2g}$ zero phonon line indicates that the coordination surrounding of the Mn^{4+} ion deviates considerably from inversion symmetry. This is in accordance with the crystal structure data. If there is a strong deviation from the center of symmetry, the ZPL becomes electric dipole-allowed and gains intensity relative to the phonon sidebands. This situation is also encountered in the distorted double perovskite Gd_2MgTiO_6 [12] and in Mg_2TiO_4 [24]. However, in the double perovskite Ba_2LaNbO_6 the intensity of the ZPL line is weaker than the phonon sidebands [25]. The energy of the $^2E \rightarrow {}^4A_{2g}$ zero phonon line in the double perovskites Ba_2LaNbO_6 (14 679 cm^{-1}) [25] and $NaLaMgTeO_6$ (14 705 cm^{-1}) is very nearly the same (Table 3). The energy position of the Mn^{4+} ^{2}E state (14 705 cm^{-1}) in $NaLaMgTeO_6$ was very well reproduced by our calculations, and the validity of our crystal field calculations is confirmed by the good agreement between the calculated energy levels of the impurity ions and the experimental data (Figs. 2 and 3).

Low-temperature decay curves of $NaLaMgTeO_6$:Mn^{4+}: Evidence for two-site occupation by the Mn^{4+} ion

In order to show that the Mn^{4+} ion simultaneously occupies both the Mg^{2+} and the Te^{6+} sites of $NaLaMgTeO_6$, we measured the decay profile of the Mn^{4+} luminescence at low temperatures (Fig. 4). The Mn^{4+} luminescence exhibits a double exponential decay. From the two linear regions of the decay curves, the lifetimes $\tau_1 = 1.09 \pm 0.01$ and $\tau_2 = 2.61 \pm 0.03$ ms were determined under 350 nm excitation, and $\tau_1 = 1.05 \pm 0.01$ and $\tau_2 = 2.45 \pm 0.03$ under 492 nm excitation. These results are taken to indicate that there are two types of sites for the Mn^{4+} ion in the perovskite structure. The obvious possibility is the simultaneous

occupation of the two *B*-site cations by the Mn^{4+} ions which has the advantage of attaining charge compensation. This substitution is also driven by the similar ionic radii of the host structure *B*-cations and that of the Mn^{4+} ion. The faster decay component probably reflects the energy transfer from the Mn^{4+} ion which occupies a high-energy site to the Mn^{4+} ion at the lower energy site which is characterized by the longer decay constant. Site selective laser excitation techniques which can differentiate between the two sites are beyond the scope of this study. This, for example, has been accomplished for the Mn^{4+} ion in the $Gd_3Ga_5O_{12}$ (GGG) garnet material [26].

The variations in the physical parameters, 10Dq and B and the energy of the $^2E_g \rightarrow {}^4A_{2g}$ emission transition in some perovskites

In this section we present an approach that allows for establishing a correlation between the energy position of the Mn^{4+} ^2E state and the values of the Racah parameters (*B* and *C*) in a particular host. The values for 10D*q*, the Racah parameters *B* and *C* and the Mn^{4+}–O^{2-} bond lengths in a few perovskite host structures are assembled in Table 3. The crystal field strength (10D*q*) is given by $10Dq = E(^4A_{1g} \rightarrow {}^4T_{2g})$. In the following we will provide a generalized interpretation of the variations in the Racah parameter *B* of the perovskites. The reduction of this parameter is due to the covalent bond formation between the Mn^{4+} ion and the ligating atoms. This nephelauxetic effect is usually represented by the ratio: $\beta = B_{complex}/B_0$, where $B_0 = 1160\,cm^{-1}$ for the Mn^{4+} ion.

The reason for the Mn^{4+}–O^{2-} bonding being less covalent in $SrTiO_3$, $BaTiO_3$ and $CaZrO_3$ relative to that in the double perovskite Ba_2LaNbO_6 has been traced to the polarization of the oxygen charge density within the [–Mn^{4+}–O^{2-}–B^{4+}–] linkage of the perovskite structure towards the B^{4+}cations (Ti^{4+} and Zr^{4+}). This is because these cations offer empty nd^0 orbitals for combination with the O^{2-} 2*p* orbitals [27 – 29]. This polarization of the charge density reduces the overlap between the Mn^{4+} 3*d* orbitals and the 2*p* O^{2-} orbitals. Thus the covalence of the Mn^{4+}–O^{2-} bonding in the three perovskites, $SrTiO_3$, $BaTiO_3$ and $CaZrO_3$ is reduced. The double perovskite Ba_2LaNbO_6 also contains Nb^{5+} cations with empty [Kr] $4d^0$ orbitals. However, the Mn^{4+}–O^{2-} bonding is relatively more covalent for the following reason. In this structure there are linkages of the type [–La^{3+}–O^{2-}–Nb^{5+}–O^{2-}–La^{3+}–] because there is an ordering between the Nb^{5+} and La^{3+} ions on the *B* site. Thus when the Mn^{4+} replaces Nb^{5+} cations, the polarization effect which shifts the center of the negative charge density of the O^{2-} ion towards the Ti^{4+}/Zr^{4+} cations and renders the Mn^{4+}–O^{2-} bonding more ionic in the perovskites $SrTiO_3$, $BaTiO_3$ and $CaZrO_3$ is absent in the double perovskite Ba_2LaNbO_6. This explains the relatively higher covalence of the Mn^{4+}–O^{2-} bonding in the double perovskite.

According to the data presented in Table 3, the Mn^{4+}–O^{2-} bonding is the least covalent in the double perovskite $NaLaMgTeO_6$. The value of $B = 790\,cm^{-1}$ indicates a relatively high ionic character of the Mn^{4+}–O^{2-} bonding in this perovskite despite the fact that there are no cations with empty orbitals that are available for combination with the oxygen 2*p* orbitals.

Table 3. Racah parameters (*B*, *C*), nephelauxetic ratio (β), crystal field splitting (D*q*), energy of the $^2E_g \rightarrow {}^4A_{2g}$ emission transition (E:^2E_g) and Mn^{4+}–O^{2-} distances (Å) in perovskites. In $NaLaMgTeO_6$, the site that is occupied by the Mn^{4+} ion is indicated in bold.

Perovskite	*B* (cm^{-1})	*C* (cm^{-1})	$\beta = B/B_0$	C/C_0	D*q* (cm^{-1})	E:^2E_g (cm^{-1})	Mn^{4+}–O^{2-} bond length (Å)	E:^2E_g calcd., Eq. 6 (cm^{-1})	Reference
Ba_2LaNbO_6	670	3290	0.57	0.76	1780	14 679	1.9973	14 874	[4, 25]
$LaAlO_3$	695	2941	0.60	0.68	2123	14 034	1.90	14 051	[6]
$YAlO_3$	720	3025	0.62	0.70	2083	14 356	1.911	14 466	[8]
$SrTiO_3$	735	2812	0.63	0.65	1820	13 792	1.951	13 849	[9]
$BaTiO_3$	738	2820	0.64	0.66	1780	13 861	2.003	13 880	[10]
$CaZrO_3$	754	3173	0.65	0.74	1850	15 054	2.096	15 081	[11]
$NaLa\mathbf{Mg}TeO_6$	790	2881	0.68	0.67	2008	14 705	2.0405	14 469	this work
$NaLaMg\mathbf{Te}O_6$	790	2949	0.68	0.69	2008	14 705	1.943	14 676	this work

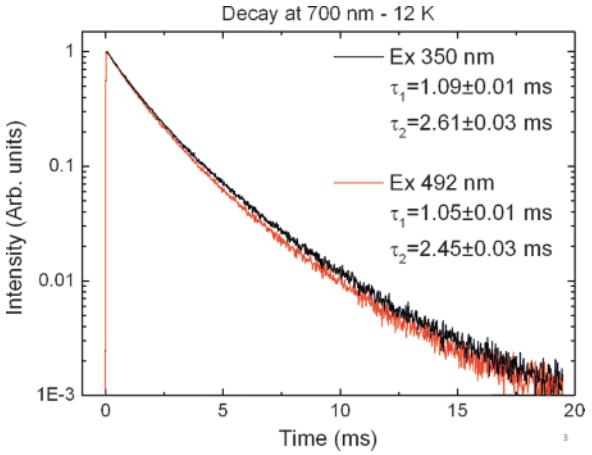

Fig. 4. Fluorescence decay at $T = 12\,K$ of $NaLaMgTeO_6:Mn^{4+}$ showing the non-exponential behavior under $\lambda_{ex} = 350\,nm$ and $\lambda_{ex} = 492\,nm$ excitation. The derived lifetimes from the decay curves are also given.

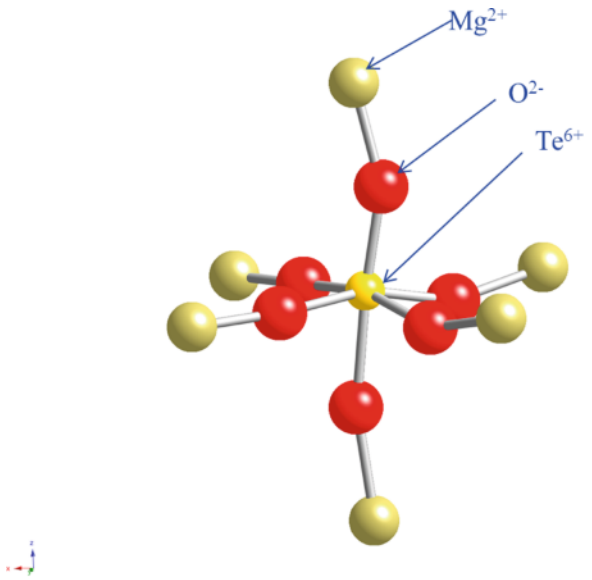

Fig. 5. The $[–Mg^{2+}–O^{2-}–Te^{6+}–O^{2-}–Mg^{2+}–]$ linkage in the double perovskite $NaLaMgTeO_6$.

This can be explained as follows. In the crystal structure of this perovskite there are linkages of the type $[–Mg^{2+}–O^{2-}–Te^{6+}–O^{2-}–Mg^{2+}–]$ (see Fig. 5). We have recently conducted *ab inito* studies on $NaLaMgTeO_6$ with the intention of exploring quantitatively the role of the host structure in determining the optical properties of the embedded activator ions. In that study we calculated the effective charges

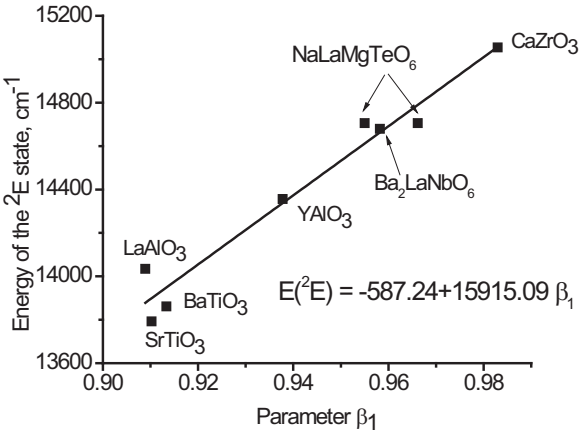

Fig. 6. The relationship between the energy of the ^2E_g state and the β_1 parameter (see text for further details).

(Mulliken charge) on all the host structure cations. It is well known that due to chemical bonding the effective charge on the cations can be significantly different from their formal charges. The effective charges of the Mg^{2+} and Te^{6+} [[Kr]$4d^{10}$] cations were determined to be (in units of proton charge; LDA results) +1.81 and +2.36, respectively. This result shows that the effective charge of the Te^{6+} cation is significantly reduced from +6 to +2.36 due to chemical bond formation. Thus the $Te^{6+}–O^{2-}$ bonding has considerable covalent character in $NaLaMgTeO_6$. This means that within linkages of the type $[–Mn^{4+}–O^{2-}–Te^{6+}–]$, the high covalency of the $Te^{6+}–O^{2-}$ bonding will render the corresponding $Mn^{4+}–O^{2-}$ bonding ionic by the inductive effect. This peculiarity of chemical bonding explains the high ionic nature of the $Mn^{4+}–O^{2-}$ bonding in the double perovskite $NaLaMgTeO_6$.

Finally, the energy of the $^2E_g \rightarrow {}^4A_{2g}$ emission in the perovskites is considered in terms of the theory of Tanabe and Sugano [7] which relates the energy of this transition to the covalence of the "Mn^{4+}–Ligand" bonding in a solid. The peak emission energy is dependent on the two Racah parameters B and C. Regarding the Mn^{4+} ion, we have recently introduced a non-dimensional parameter, $\beta_1 = \sqrt{\left(\frac{B}{B_0}\right)^2 + \left(\frac{C}{C_0}\right)^2}$, which relates the energy of the $^2E_g \rightarrow {}^4A_{2g}$ transition to the Racah parameters $B$and C [6]. The subscript "0" refers to the values of the Racah parameters for the free Mn^{4+} ion ($B_0 = 1160\,cm^{-1}$ and $C_0 = 4303\,cm^{-1}$) [30]. Fig. 6 shows that the peak emission energy of the

$^2E_g \rightarrow {}^4A_{2g}$ transition in the perovskites of Table 3 is linearly related to β_1 showing that any description of the nephelauxetic effect for the Mn^{4+} containing hosts must consider both Racah parameters B and C.

In reference [31], another equation has been proposed which links the energy of the ^2E_g state of the d^3 electron configuration with the Dq:

$$E(^2E_g)/B = 3.05C/B + 7.90 - 1.80B/Dq. \quad (5)$$

The energy of the ^2E_g state calculated using Eq. 5 is also listed in Table 3. As seen from the Table, both experimental and estimated values of the ^2E_g state position match each other well. We must point out that Eq. 5, strictly speaking, is valid only for cubic symmetry and does not reflect any effect of a low-symmetry component of a crystal field, which must eventually lead to the splitting of the orbitally degenerated energy levels.

Conclusions

In this work we have evaluated the UV/Vis spectroscopic properties of the Mn^{4+} ion in $NaLaMgTeO_6$, a material which crystallizes with a distorted perovskite structure and exhibits ordering of both A-site and the B-site cations. Evidence is presented for the occupation by the Mn^{4+} ion of both the six-coordinated Mg^{2+} and Te^{6+} sites of the host structure. We have calculated the energy levels of the Mn^{4+} ion using the exchange charge model of crystal field theory and demonstrated that the results of our calculations are in good agreement with the experimental data. Our interpretation of the variations in the Racah parameter B in the perovskite family of materials is based on the changes in the covalent character of the Mn^{4+}–O^{2-} bonding which is driven by the cationic substructure that occurs in the corner-linked BX_6 octahedral moieties.

Acknowledgement

M. G. Brik acknowledges support from the European Social Fund's Doctoral Studies and Internationalisation Programme DoRa, the European Union through the European Regional Development Fund (Center of Excellence "Mesosystems: Theory and Applications", TK114) and the Marie Curie Initial Training Network LUMINET, grant agreement no. 316906.

[1] M. G. Brik, A. M. Srivastava, *J. Lumin.* **2013**, *133*, 69 – 72.
[2] M. G. Brik, A. M. Srivastava, N. M. Avram, *Opt. Mater.* **2011**, *33*, 1671 – 1676.
[3] A. M. Srivastava, M. G. Brik, *Opt. Mater.* **2012**, *35*, 196 – 200.
[4] A. M. Srivastava, M. G. Brik, *J. Lumin.* **2012**, *132*, 579 – 584.
[5] M. G. Brik, A. M. Srivastava, *Opt. Mater.* **2013**, *35*, 1251 – 1256.
[6] A. M. Srivastava, M. G. Brik, *Opt. Mater.* **2013**, *35*, 1544 – 1548.
[7] Y. Tanabe, S. Sugano, *J. Phys. Soc. Jpn.* **1954**, *9*, 753 – 766.
[8] M. G. Brik, I. Sildos, M. Berkowski, A. Suchocki, *J. Phys.: Condensed Matter* **2009**, *21*, 025404.
[9] M. G. Brik, N. M. Avram, *J. Phys.: Condensed Matter* **2009**, *21*, 155502.
[10] X.-X. Wu, W. Fang, W.-L. Feng, W.-C. Zheng, *Pramana – J. Phys.* **2009**, *72*, 569 – 575.
[11] M. G. Brik, A. M. Srivastava, *ECS J. Solid State Sci. Technol.* **2013**, *2*, R148–R152.
[12] A. M. Srivastava, W. W. Beers, *J. Electrochem. Soc.* **1996**, *143*, L203–L205.
[13] M. L. Lopez, M. L. Veiga, C. Pico, *J. Mater. Chem.* **1994**, *4*, 547 – 550.
[14] K. Momma, F. Izumi, *J. Appl. Crystallogr.* **2011**, *44*, 1272 – 1276.
[15] G. King, P. M. Woodward, *J. Mater. Chem.* **2010**, *20*, 5785 – 5796.
[16] M. C. Knapp, P. M. Woodward, *J. Solid State Chem.* **2006**, *179*, 1076 – 1085.
[17] R. D. Shannon, *Acta Crystallogr.* **1976**, *A32*, 751 – 767.
[18] B. Z. Malkin in *Spectroscopy of Solids Containing Rare-Earth Ions*, (Eds.: A. A. Kaplyanskii, B. M. Macfarlane), North-Holland, Amsterdam, **1987**, p. 33 – 50.
[19] B. Z. Malkin, T. T. A. Lummen, P. H. M. van Loosdrecht, G. Dhalenne, A. R. Zakirov, *J. Phys.: Condensed Matter* **2010**, *22*, 276003.
[20] E. Clementi, C. Roetti, *At. Data Nucl. Data Tables* **1974**, *14*, 177 – 478.
[21] M. V. Eremin in *Spectroscopy of Crystals*, (Ed.: A. A. Kaplyanskii), Moscow, **1989**, pp. 30 – 44 (in Russian).
[22] W. M. A. Smit, G. Blasse, *J. Solid State Chem.* **1986**, *63*, 308 – 315.
[23] M. A. Hamstra, H. F. Folkerts, G. Blasse, *Mater. Res. Bull.* **1995**, *30*, 93 – 96.

[24] L. G. J. De Haart, A. J. De Vries, G. Blasse, *J. Solid State Chem.* **1985**, *59*, 291 – 300.
[25] P. A. Tanner, Z. Pan, *Inorg. Chem.* **2009**, *48*, 11142 – 11146.
[26] A. Brenier, A. Suchocki, C. Pedrini, G. Boulon, C. Madej, *Phys. Rev. B* **1992**, *46*, 3219 – 3227.
[27] A. M. Srivastava, *Opt. Mater.* **2009**, *31*, 881 – 885.
[28] A. M. Srivastava, *J. Lumin.* **2009**, *129*, 1000 – 1002.
[29] A. M. Srivastava, M. G. Brik, *J. Lumin.* **2010**, *130*, 2368 – 2376.
[30] P. H. M. Uylings, A. J. J. Raassen, J. F. Wyart, *J. Phys. B: At. Mol. Phys.* **1984**, *17*, 4103 – 4126.
[31] B. Henderson, G. F. Imbusch, *Optical Spectroscopy of Inorganic Solids*, Clarendon Press, Oxford, **1989**.